Isotope scattering and phonon thermal conductivity in light atom compounds: LiH and LiF

L. Lindsay

Materials Science and Technology Division, Oak Ridge National Laboratory, Oak Ridge, Tennessee 37831, USA

(Received 25 August 2016; revised manuscript received 17 October 2016; published 8 November 2016)

Engineered isotope variation is a pathway toward modulating lattice thermal conductivity (κ) of a material through changes in phonon-isotope scattering. The effects of isotope variation on intrinsic thermal resistance is little explored, as varying isotopes have relatively small differences in mass and thus do not affect bulk phonon dispersions. However, for light elements, isotope mass variation can be relatively large (e.g., hydrogen and deuterium). Using a first principles Peierls-Boltzmann transport equation approach, the effects of isotope variance on lattice thermal transport in ultra-low-mass compound materials LiH and LiF are characterized. The isotope mass variance modifies the intrinsic thermal resistance via modulation of acoustic and optic phonon frequencies, while phonon-isotope scattering from mass disorder plays only a minor role. This leads to some unusual cases where κ values of isotopically pure systems (^{6}LiH,^{7}Li^{2}H, and ^{6}LiF) are lower than the values from their counterparts with naturally occurring isotopes and phonon-isotope scattering. However, these κ differences are relatively small. The effects of temperature-driven lattice expansion on phonon dispersions and calculated κ are also discussed. This paper provides insight into lattice thermal conductivity modulation with mass variation and the interplay of intrinsic phonon-phonon and phonon-isotope scattering in interesting light atom systems.

DOI: 10.1103/PhysRevB.94.174304

I. INTRODUCTION

Isotopes of various materials have played critical roles in the development and advancement of scores of technologies that we now take for granted. For example, isotopic enrichment of Uranium (^{235}U) and Plutonium (^{239}Pu) was critical for developing nuclear fission technologies, various isotopes are used as radioactive tracers to study physiological processes (e.g., ^{123}I), and radioisotopes (e.g., ^{241}Am) are key ingredients in millions of smoke detectors around the world. Typically, these technologies rely on radioactive decay of meta-stable isotopes, most often with large numbers of protons and neutrons. However, even light atoms can be useful radioisotopes: Positron emission tomography (PET) cancer scans use ^{18}F as a positron emitter, and radioactive dating, typically examining ^{14}C concentrations, is used to determine the age of materials important for archaeologic studies and examining geologic history.

Varying isotopes can also be interesting and technologically useful beyond radioactive decay. Of interest here are the effects of isotopic variations on thermal conductivity (κ) in semiconductors and insulators as they alter the transport of thermal energy via lattice vibrations and phonons. These phonons scatter from mass perturbations in the crystal such as isotope variation. Thus, depending on the temperature (T) regime and relative strengths of other phonon scattering mechanisms, isotopes can play a critical role in determining thermal transport in a material. For example, a peak value in κ as a function of temperature [$\kappa(T)$] occurs in Ge for $T \sim 20$ K where point defects such as isotope mass variance are important. Isotopically purified crystals of Ge were shown to have a threefold increase in κ at this temperature [1]. Even at room temperature, diamond [2,3], BN nanotubes [4], and graphene [5] have large enhancements to κ with isotope purification, and calculations predict large enhancements to κ in some compound materials: GaN [6], BeSe, and GeC [7].

The focus of this paper is not just on the relative importance of phonon-isotope scattering but also on the interplay of this scattering with changes that mass variance gives to the intrinsic phonon-phonon scattering via modulation of the phonon dispersion. Phonon frequencies critically depend on the masses of the constituent elements. In a multicomponent material, optic phonon branches are generally governed by light atoms, while acoustic branches are governed by the heaviest atoms. Decreasing the mass of either drives the corresponding phonon branches to higher frequencies, while the opposite is true for increasing mass. Thus, isotope variation can be employed to manipulate the phonon spectrum [8], though frequency changes are typically small and likely have very little effect on the intrinsic scattering. In fact, calculations of isotope modulated κ typically model the effects of isotope variance by simply introducing mass perturbation scattering [9–11], without consideration of phonon frequency modulation. Here we address the following questions. *Can frequency changes with isotope variation significantly manipulate intrinsic thermal resistance? More specifically, can higher κ be achieved in systems with more mass disorder? Can acoustic modes be appreciably altered by isotope modification, e.g., modulated sound velocities?*

Such properties require systems for which the constituent elements have small mass so that isotope variation can give relatively large changes to the nuclear masses, e.g., ultra-small-mass rock salt compounds LiH and LiF, both of which have a significant amount of measured data for both dispersions and κ. Natural isotopic variance of Li is 7.6% ^{6}Li and 92.4% ^{7}Li, while H and F are virtually pure ^{1}H and ^{19}F. Isotopically modifying light atom materials is fairly inexpensive, thus incorporating varying amounts of ^{2}H (deuterium), ^{6}Li, and ^{7}Li in these systems is not unreasonable. LiH is often considered for energy storage technologies and shielding in nuclear reactors [12]; an isotope variant, ^{6}Li^{2}H, is used as fusion material in thermonuclear weapons. LiF is used in radiation detection [13] and ultraviolet optics [14], and LiF salts are used as solvents in nuclear reactors [15].

In this paper, we will examine κ and isotope variation of κ by both phonon-mass defect scattering and modification of the phonon dispersions. This paper is organized as follows. Section II outlines the theoretical methods employed. Section III gives the Results and Discussion: comparison with measured data and physical analysis. Section IV gives the conclusions, and an Appendix gives further theoretical methods and phonon dispersion data.

II. THEORY

We employ a full solution to the steady-state Boltzmann-Peierls phonon transport equation (BPE), $\vec{v}_{\vec{q}j} \cdot \vec{\nabla} T(\partial n_{\vec{q}j}/\partial T) = (\partial n_{\vec{q}j}/\partial t)_{\text{scatter}}$, to determine the nonequilibrium phonon distributions $n_{\vec{q}j}$ arising from an applied temperature gradient $\vec{\nabla} T$ [16–18] in a homogeneous system. Here, $\vec{v}_{\vec{q}j}$ is the phonon velocity for phonon mode with wave vector $\vec{q}$ in branch j. We assume $n_{\vec{q}j}$ is the equilibrium Bose distribution $n^0_{\vec{q}j}$ plus a deviation linear in $\vec{\nabla} T$. This deviation determines the transport lifetimes $\tau_{\vec{q}j,\alpha}$ in Cartesian direction α coinciding with the direction of the temperature gradient. These enter the equation for the lattice thermal conductivity:

$$\kappa_{\alpha\beta} = \sum_{\vec{q}j} C_{\vec{q}j} v_{\vec{q}j,\alpha} v_{\vec{q}j,\beta} \tau_{\vec{q}j,\alpha}, \tag{1}$$

with $C_{\vec{q}j}$ being the volume normalized mode specific heat and $v_{\vec{q}j,\alpha}$ being the αth component of the velocity. For the rock salt structures considered here, the thermal conductivity tensor can be described by a single component: $\kappa_{xx} = \kappa_{yy} = \kappa_{zz} = \kappa$; off-diagonal terms are zero. For calculations presented here, the scattering term on the right hand side of the BPE is constructed from combinations of intrinsic anharmonic three-phonon scattering [17,18] (lowest order in perturbation theory), phonon-isotope scattering [9–11], and phonon-boundary scattering [17,19]. Further details of the scattering rate calculations have been described previously [6,7,17,18]. The BPE is then solved self-consistently [20,21], beyond the relaxation time approximation (RTA). Phonon-boundary scattering rates (when included) were determined by $1/\tau^{p-b}_{\vec{q}j} = |\vec{v}_{\vec{q}j}|/L$ with L, system size, empirically chosen to fit the ultra-low temperature κ data for each system. We note that boundaries play a role only in determining κ below temperature $T \sim 10-20$ K, also below the conductivity peaks. Like the intrinsic three-phonon scattering, the phonon-isotope scattering is derived from quantum mechanical perturbation theory [9–11] and has no adjustable fitting parameters.

Besides trivial terms such as atomic masses and isotope concentrations, harmonic and third-order anharmonic interatomic force constants (IFCs), or potential derivatives, are the only required inputs for the calculations. The harmonic IFCs are determined from density functional perturbation theory [22] using the Quantum Espresso (QE) package [23,24] with 100 Ry energy cutoff for the wave functions, $12 \times 12 \times 12$ q-point mesh for the electronic structure, and $8 \times 8 \times 8$ k-point mesh for linear response calculations. The anharmonic IFCs are calculated to fifth nearest neighbor of the unit cell atoms via numerical derivatives determined from Hellman-Feynman forces from perturbations of 216 atom supercells using density functional theory [25,26], as implemented by the QE package. The Γ-point only calculations were employed, also with a 100 Ry energy cutoff for the wave functions. For these calculations, the norm-conserving Troullier-Martins pseudopotential method [27] was employed to characterize the core electrons. The generalized gradient approximation (GGA) and the local density approximation (LDA) were both employed. Input files and calculated IFCs can be found in the Supplemental Material [28].

As phonon dispersions play a critical role in determining thermal transport, some care was taken to determine the best DFT formalism to describe LiH and LiF systems. Each structure was relaxed by adjusting the lattice constant (a) to find the lowest calculated electronic energy for both LDA and GGA. For all cases, the calculated a values were smaller than experiment: for LiH, $a_{\text{LDA}} = 3.894$ Å, $a_{\text{GGA}} = 3.947$ Å, $a_{\text{exp}} = 4.083$ Å [29] and for LiF, $a_{\text{LDA}} = 3.886$ Å, $a_{\text{GGA}} = 4.005$ Å, $a_{\text{exp}} = 4.02$ Å [30]. Experimental lattice parameters were measured at room temperature. For the GGA calculations this is surprising, as they typically underbind atoms (LDA tends to overbind atoms) [31]. For Li^2H, the resulting GGA phonon dispersion gives reasonable agreement with measured data for Li^2H (Fig. 10 in the Appendix), while the LDA does a poor job describing the acoustic modes. For LiF, both the calculated LDA and GGA dispersions fail to describe the longitudinal acoustic and low frequency optic modes accurately (Fig. 11 in the Appendix).

The measured a values and dispersions were taken at room temperature, while DFT calculations are for ground state zero temperature systems. We examined the effects of temperature on a and the dispersions for the LDA calculations within the quasiharmonic approximation using the following expression for temperature dependent lattice parameter, $a(T)$ [32]:

$$a(T) = a_0 \left[1 + \frac{1}{3 V_0 B} \sum_{\vec{q}j} \gamma_{\vec{q}j} \hbar \omega_{\vec{q}j} \left(n^0_{\vec{q}j} + \frac{1}{2} \right) \right]. \tag{2}$$

This includes zero-point motion of the atoms and thermal shifts due to vibrational energy. a_0 and V_0 are calculated lattice parameter and volume at equilibrium ($T = 0$ K), respectively; B is the bulk modulus ($B = 31.7$ GPa for Li^2H from Ref. [33] and $B = 67.1$ GPa for LiF from Ref. [34]); $\omega_{\vec{q}j}$ is phonon frequency; and $\gamma_{\vec{q}j}$ is the mode dependent Grüneisen parameter defined in the Appendix. We note that including lattice expansion for the GGA calculations gives worse agreement with measured phonon dispersion data, and thus only the LDA is considered further. Figure 1 gives $a(T)/a_0$ for LiH, Li^2H, and LiF versus temperature; this is also given for GaAs for comparison. LiH and LiF have significant zero point motion effects (curves do not go to one at $T = 0$) [32], and $a(T)$ varies substantially with T when compared with GaAs, a typical zincblende material. Further, there is variation of the LiH and Li^2H curves as the phonon frequencies, and thus the vibrational energies depend on the isotopic mass [32]. The lattice expansion does not give a (300 K), in agreement with measured data; however, using harmonic IFCs calculated for a (300 K) gives better agreement with measured dispersions for both Li^2H (Fig. 10 in the Appendix) and LiF (Fig. 11 in the

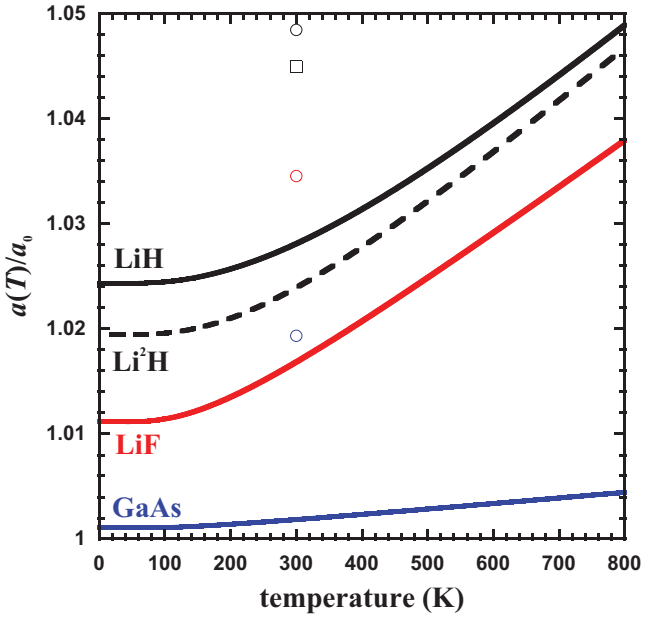

FIG. 1. Calculated LDA $a(T)/a_0$ versus temperature of LiH (solid black curve), Li^2H (dashed black curve), LiF (red curve), and GaAs (blue curve). The calculated equilibrium lattice parameters a_0 are 3.894 Å, 3.894 Å, 3.886 Å, and 5.546 Å for LiH, Li^2H, LiF, and GaAs, respectively. Room temperature measured lattice constants scaled by the calculated a_0 values are given for LiH (black circle) [29], Li^2H (black square) [29], LiF (red circle) [30], and GaAs (blue circle) [35]. Note that the curves do not approach one at $T = 0$ due to zero point motion of the atoms [32].

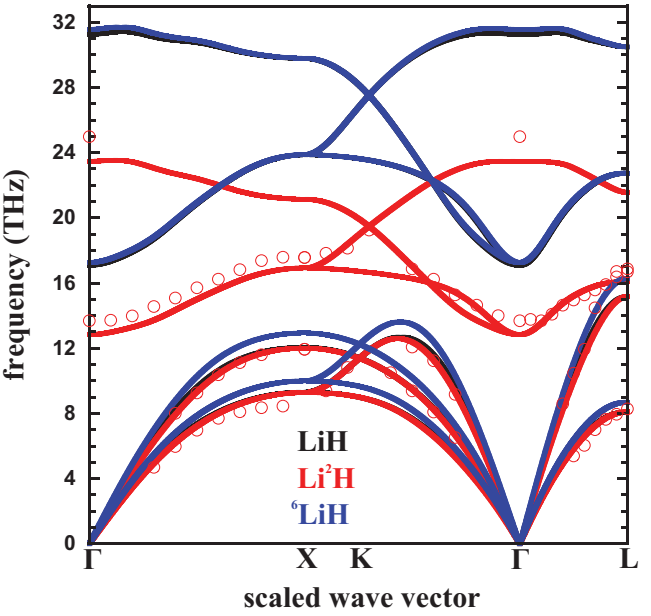

FIG. 2. Calculated phonon dispersions in high symmetry directions for LiH (black curves) and Li^2H (red curves) with natural isotope averaged Li mass and for ^{6}LiH (blue curves). ^{2}H is also known as deuterium. Red circles give measured Li^2H data [36]. Calculations were done with LDA and a (300 K), as described in the text. The black curves are difficult to distinguish as they nearly coincide with the blue curves (^{6}LiH) for the optic frequencies and with the red curves (Li^2H) for the acoustic frequencies.

Appendix). For the rest of this paper, we employ harmonic and anharmonic IFCs determined from LDA calculations using a (300 K) values for LiH (4.004 Å) and LiF (3.951 Å).

III. RESULTS AND DISCUSSION

A. Comparison with experiment

First, we examine the phonon dispersions of LiH and LiF with different isotope concentrations, given by Fig. 2 and Fig. 3, respectively. When the mass number is not given here the natural isotope averaged mass is used. Typically, small variations in mass (m) given by different isotopes in a material have very little effect on the phonon frequencies, though they may play a role in phonon scattering from mass disorder. However, for these light atom systems, isotope mass differences alter the dispersions significantly as the relative mass changes are fairly large: $m(^2\text{H})/m(^1\text{H}) = 2.00$ and $m(\text{Li})/m(^6\text{Li}) = 1.15$.

The most dramatic frequency changes occur for the optic modes of LiH when replacing ^{1}H (black curves) with ^{2}H (red curves), as seen in Fig. 2. The black curves are difficult to distinguish as they nearly coincide with the blue curves (^{6}LiH) for the optic frequencies and with the red curves (Li^2H) for the acoustic frequencies. The optic phonon frequencies of LiH are 33–41% higher than those of Li^2H. Note that lighter atoms shift phonons to higher frequencies, while heavier atoms shift phonons to lower frequencies. The optic modes are predominantly governed by motion of the light atoms and acoustic modes by motion of the heavy atoms. Thus, very little change is observed for the acoustic branches in LiH and Li^2H. However, when comparing the acoustic modes of LiH (black curves) with those of ^{6}LiH (blue curves), there are

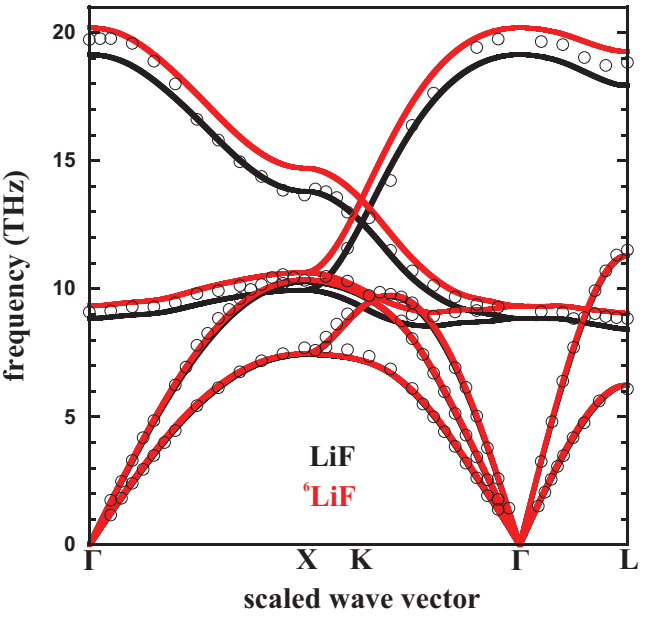

FIG. 3. Calculated phonon dispersions in high symmetry directions for LiF (black curves) and ^{6}LiF (red curves). Black circles give measured data for LiF [37]. Calculations were done with LDA and a (300 K), as described in the text.

TABLE I. Calculated thermal conductivity κ, Debye temperature θ_D, and optic bandwidth given by $(\omega^o_{max} - \omega^o_{min})/\omega^a_{max}$ for each LiH and LiF system. Here, ω^o_{max}, ω^o_{min}, and ω^a_{max} are calculated maximum optic, minimum optic, and maximum acoustic frequencies, respectively. All calculations are done using LDA and a (300 K), as described in the text. The unit cell mass (M_{cell}) of each system is also given.

	θ_D(K)	M_{cell}(amu)	Scaled optic bandwidth	κ (W/m-K)
LiH	1202	7.95	0.94	23.00
^{7}LiH	1197	8.02	0.95	24.15
^{6}LiH	1279	7.02	0.88	22.88
Li^{2}H	1133	8.96	0.70	13.44
^{7}Li^{2}H	1129	9.03	0.71	12.82
^{6}Li^{2}H	1197	8.03	0.67	14.54
LiF	802	25.94	1.06	14.58
^{7}LiF	801	26.01	1.06	14.92
^{6}LiF	817	25.01	1.08	13.49

appreciable differences, 6–7% for all of the acoustic modes. These differences can also be found in the Debye temperatures θ_D (see Table I), which are calculated from the acoustic sound velocities (see Appendix). This is unusual, again, because the acoustic modes are governed by the heavy atoms, which have less relative isotope mass variation than lighter atoms in typical systems. Comparing the phonon dispersions of LiF with those of ^{6}LiF in Fig. 3, the acoustic modes are unchanged as Li is the lighter atom in this system, while the optic modes are shifted higher by 5–7%. Again, phonon lifetimes and conductivity depend critically on features of the dispersion. One might expect that ^{6}LiH will have higher calculated κ than LiH given that the heat-carrying acoustic phonons have higher velocities and that there is no mass disorder scattering in ^{6}LiH; however, this is not the case (see Table I) due to changes in the intrinsic phonon scattering rates, as explained later.

Next, we present a comparison of calculated coefficients of linear thermal expansion (α) with measured values as a function of temperature in Fig. 4 for LiH (black curve), Li^{2}H (red curve), and LiF (green curve). α is defined by Eq. (A1) in the Appendix and is a function of both the harmonic and anharmonic IFCs. Thus, the general agreement between the calculated and measured α gives confidence that the IFCs give a good representation of the anharmonicity of these systems, as the agreement of the calculated and measured phonon dispersions gives confidence in the harmonic properties. The cause for the relatively worse agreement for measured and calculated α of LiF compared to those of the LiH systems is unknown.

Figures 5 and 6 give the calculated κ values for various isotope concentrations of LiH and LiF, respectively, over a wide range of temperature compared to measured data. The low T data ($T < 20$ K) is not fully first principles, as the calculated κ was fit to match experiment at 3 K in each case by adjusting L (system size) in the empirical phonon-boundary scattering term described previously. The L values for LiH systems are the following: LiH: 0.175 mm; Li^{2}H: 0.150 mm (black and red curves in Fig. 5, respectively). The L values for LiF systems are the following: 99.99% ^{7}Li : 10 mm; 97.2% ^{7}Li : 8 mm; 92.41% ^{7}Li : 7 mm; 50.8% ^{7}Li : 7 mm; and 9.6% ^{7}Li : 5 mm (black, red, green, purple, and orange

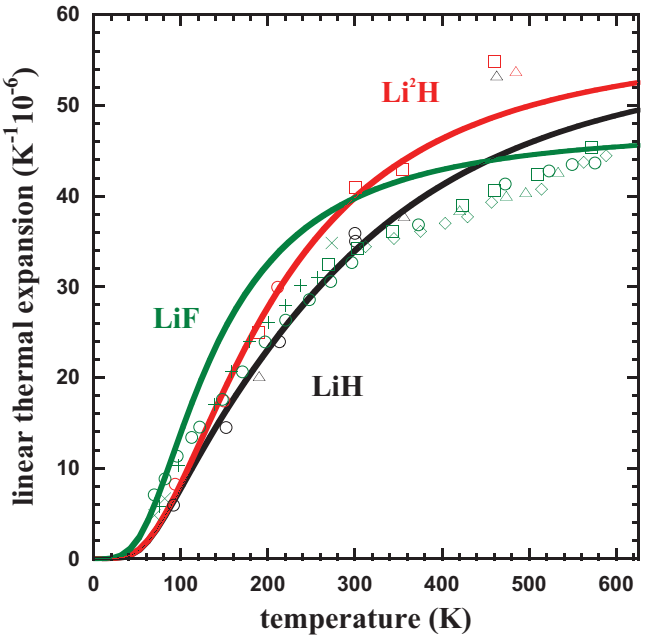

FIG. 4. Calculated coefficient of linear thermal expansion [40] versus temperature for LiH (black curve), Li^{2}H (red curve), and LiF (green curve) compared with experimental measurements (note that error bars for the measurements are not shown). Measured data for LiH (black circles [39], black triangles [29]) and Li^{2}H (red circles [39], red squares [29], and red triangle [41]) from references in Ref. [38] and for LiF from Ref. [42] (green circles) and references therein (green triangles [43], green squares [44], green diamonds [45], green Xs [46], and green crosses [47]).

curves in Fig. 6, respectively). For the LiF systems, these sizes are larger than that of the samples from experiment (5–7 mm) [52,53], though in reasonable agreement given the crudeness of the phonon-boundary scattering model. For LiH, L is remarkably smaller than the sample dimensions, ~2.5 mm [48]. This will be discussed in more detail below. The κ calculations for $T < 10$ K included only phonon-boundary and phonon-isotope scattering, as convergence with integration grid density was prohibitively costly with inclusion of the intrinsic scattering as more sampling of the lower frequency acoustic phonons is required. For $T > 10$ K, the κ calculations converged with much lower integration grids, and thus all scattering mechanisms were included. The curves in the intermediate temperature regime around 10 K overlapped reasonably well, as can be seen by the lack of discontinuity of the calculated curves in Figs. 5 and 6. The intrinsic scattering rates were separately calculated for each isotope variation as this gives significant differences in phonon dispersions. Again, this is typically ignored in calculations of isotopically modified κ, though it is considered in some calculations of κ in alloyed material (mixing of elements with differing proton number) within the virtual crystal approximation [56,57]. We note that changes in the calculated IFCs are not considered with variation of neutron number.

All calculated curves show the same general and expected $\kappa(T)$ trends (as does the measured data for the most part):

Boundary scattering regime. At low $T(< 10$ K),$\kappa(T)$ is dominated by phonon-boundary scattering and $\kappa(T) \sim T^3$

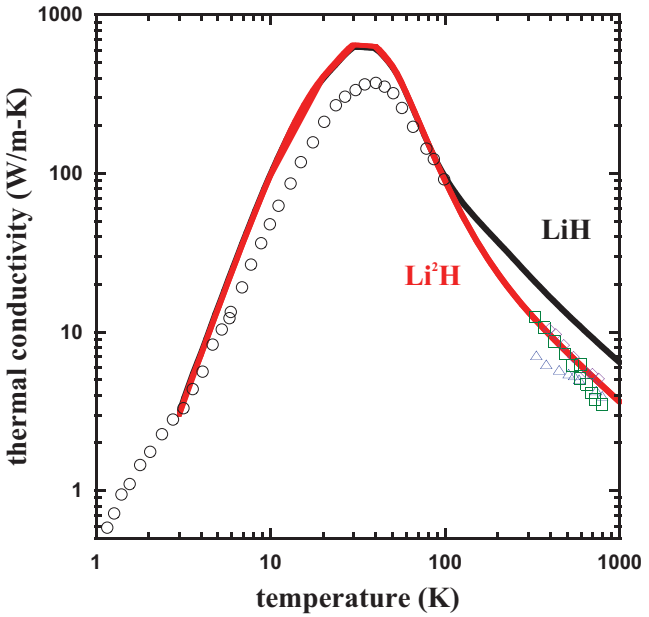

FIG. 5. Calculated κ versus temperature for LiH (black curve) and Li^2H (red curve) with naturally occurring Li abundances. Phonon-boundary, phonon-isotope, and phonon-boundary scattering are included for $T > 10$ K, while only phonon-boundary and phonon-isotope scattering are considered for $T < 10$ K. The system size, L, for the phonon-boundary scattering was 0.175 mm and 0.150 mm for LiH and Li^2H, respectively. Low T measured κ data for LiH are given by black circles and are from unpublished data in Ref. [48]. High T measured κ data are given by green squares [49], blue triangles [50], and purple diamonds [51], also obtained from Ref. [48]. The red and black curves are nearly identical for $T < 100$ K, as the only differences in κ arise from acoustic-optic phonon scatterings, which become "frozen out" with decreasing T.

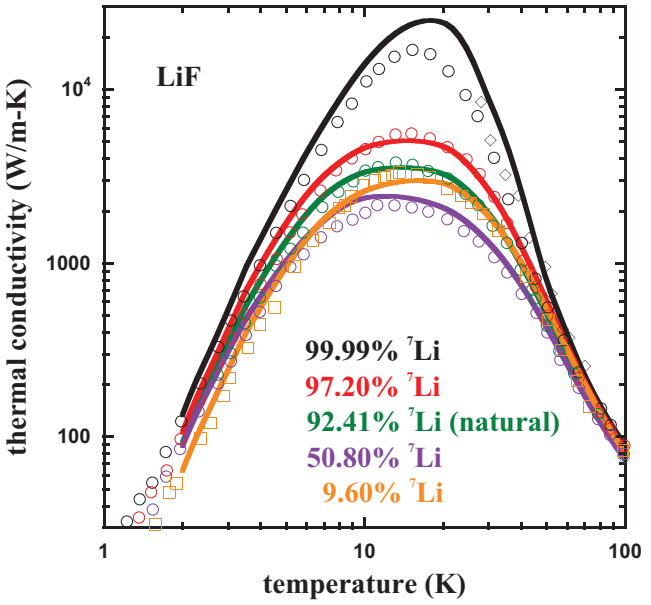

FIG. 6. Calculated κ versus temperature for LiF with differing Li concentrations: 99.99% ^{7}Li (black curve), 97.2% ^{7}Li (red curve), 92.41% ^{7}Li (green curve), 50.80% ^{7}Li (purple curve), and 9.6% ^{7}Li (orange curve). Measured data for the same isotope concentrations have the same corresponding colors (circles [52], squares [53], and diamonds [54]). Phonon-boundary, phonon-isotope, and phonon-boundary scattering are included for $T > 10$ K, while only phonon-boundary and phonon-isotope scattering are considered for $T < 10$ K. The system size, L, for the phonon-boundary scattering was 10 mm (black curve), 8 mm (red curve), 7 mm (green curve), 7 mm (purple curve), and 5 mm (orange curve).

with increasing T, behavior dictated by the phonon specific heat [58,59]. However, even at the lowest temperatures, the LiF systems (excluding the isotopically purified 99.99% ^{7}Li system) show signs that phonon-isotope scattering is playing a role, as the power law exponent is subcubic, $\kappa(T) \sim T^{2.50} - T^{2.85}$ depending on the isotope variance. The measured data also give subcubic temperature dependence, even for the highest purity sample. The low T measured data for LiH is quite unusual, nonlinear on log-log scales with fits to the data giving $\kappa(T) \sim T^2$ behavior. Unfortunately, little information is given about the sample and measurements in Ref. [48]. Thus, it is hard to draw definitive conclusions as to the discrepancy between the model L (0.175 mm) used here to fit the $\kappa(T)$ data and the reported sample size (~2.5 mm) [48].

Isotope scattering regime. At intermediate T (10 K < T < 75 K) phonon-isotope scattering becomes the dominant resistance, and intrinsic anharmonic scattering becomes more important. The interplay of these mechanisms determines the $\kappa(T)$ peak magnitudes and positions; stronger phonon-isotope scattering relative to the intrinsic phonon-phonon scattering suppresses the peak values and shifts the $\kappa(T)$ peaks to lower T. Both LiH systems have $\kappa(T)$ peaks at $T \sim 35$ K, while the LiF systems have peaks at $T \sim 15$ K $- 20$ K. For the LiF systems, the calculated $\kappa(T)$ curves are in agreement with measured values except for the case with 99.99% ^{7}Li (black curve) with a larger calculated peak value shifted to slightly higher T. This is indicative of the presence of other extrinsic scattering mechanisms present in the sample (e.g., point defects such as vacancies and site substitutions). The $\kappa(T)$ magnitude at the peak position is highly sensitive to extrinsic scattering, as the intrinsic anharmonic scattering is still relatively weak. Note that this calculated peak $\kappa(T)$ drops an order of magnitude when including just 3.8% ^{6}Li (red curve).

Anharmonic scattering regime. At high T (>75 K), including room temperature, anharmonic scattering is dominant with phonon-isotope scattering playing a lesser role; phonon-boundary scattering is negligible. In Fig. 7, we give calculated $\kappa(T)$ LiH (black curves), Li^2H (green curves), and LiF (red curves) with varying Li isotope concentrations: natural isotope abundance (solid curves), pure ^{7}Li (dashed curves), and pure ^{6}Li (dotted curves). The calculated curves give $\kappa(T) \sim T^{-1.0} - T^{-1.1}$ when fitting power law curves to the data for 300 K < T < 1000 K. The $\kappa(T) \sim T^{-1}$ behavior is expected when three-phonon scattering is the dominant resistance. Some of the measured $\kappa(T)$ values give $\kappa(T) \sim T^{-1.15} - T^{-1.2}$, suggesting that some other phonon scattering might be playing a role in the experiments. At high T (above the Debye temperature, near the melting point), higher order phonon scattering processes and/or further lattice expansion might play a role in determining κ [17,18,60]. Again, LDA *a*

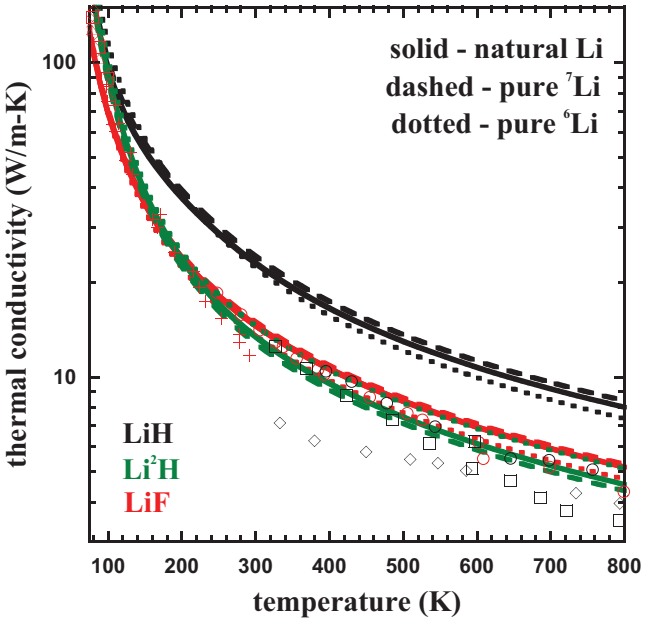

FIG. 7. Calculated κ versus temperature for LiH (black curves), Li^2H (green curves), and LiF (red curves) with different Li isotope concentrations: natural isotope abundances (solid curves), pure ^{7}Li (dashed curves), and pure ^{6}Li (dotted curves). The dashed and dotted curves include only intrinsic phonon-phonon scattering, while the solid curves include phonon-phonon and phonon-isotope scattering. Measured κ data for LiH given by black diamonds [50], black squares [49], and black circles [51] and for LiF given by red diamonds [52], red squares [52], red Xs [52], red triangles [52], red plusses [53], and red circles [55].

(300 K) values were used to determine the IFCs and κ for these calculations. The melting points of LiH and LiF are reported as ~950 K and ~1100 K, respectively. The calculated and measured κ data for LiF agree reasonably well; however, those for LiH do not. This is surprising given the good agreement with measured phonon dispersion data for Li^2H (harmonic) and thermal expansion data for LiH (anharmonic), especially in light of previous first principles calculations that found good agreement with experiment without adjustable parameters [6,56,61,62]. Around room temperature, the calculated κ of LiH is nearly two times larger than measured. This disagreement is indicative of either relatively poor sample qualities or the importance of including higher order anharmonic effects, as described above. Further, it was previously noted that the Born-Oppenheimer approximation fails in HF dimers [63]; this might also give discrepancies in the calculated properties of the ultralight LiH system here. It is interesting that the calculated $\kappa(T)$ for Li^2H is in better agreement with the measured values. Unfortunately, information of the experimental samples and techniques are difficult to obtain as most of the data is from technical government reports from decades ago [48–51].

Including higher order scattering terms (beyond three-phonon interactions) in the calculation of the intrinsic κ is beyond the scope of this paper; however, here we briefly comment on the role of thermal expansion within the quasi-harmonic approximation in determining κ. From Fig. 1, it is apparent that LiH and LiF lattice constants are more sensitive to temperature than the GaAs counter example shown, and inclusion of this lattice expansion is necessary for better agreement of calculated phonon dispersions with measured values. The same is true of κ: Using LDA IFCs generated with a_0 (lattice constant from energy minimization) gives generally higher $\kappa(T)$ than that for a (300 K), even higher than measured values. Table II gives a comparison of calculated κ values for LiH and LiF using IFCs generated with a_0, a (300 K) and a (600 K). Calculated lattice constants for LiH are $a_0 = 3.894$ Å, $a(300\text{ K}) = 4.004$ Å, and $a(600\text{ K}) = 4.048$ Å; for LiF, the constants are $a_0 = 3.886$ Å, $a(300\text{ K}) = 3.951$ Å, and $a(600\text{ K}) = 3.999$ Å. Generally, κ decreases with increasing lattice parameter as the phonon modes soften for each system. Further, including the effects of lattice expansion within this quasiharmonic approximation also gives relatively better agreement of calculated and measured κ values. For example, using a (0 K) and a (300 K) IFCs gives 22.42 and 14.59 W/m-K, respectively, for LiF at room temperature compared with the measured value 14.09 W/m-K [55].

B. Physical analysis

Thermal conductivity depends critically on details of the phonon dispersions via phonon velocities, mode specific heats, and on changes of the phase space for phonon-phonon scatterings, as dictated by conservation conditions: crystal momentum and energy. Thus, details of phonon branch shifts due to isotope modification may play a significant role in altering the intrinsic κ of these materials. First, we focus on sound velocities by examining changes in the calculated Debye temperatures constructed from these (see Eq. (A2) in the Appendix). That is, larger θ_D indicates larger acoustic velocities and, thus, typically larger κ (see velocity dependence of κ in Eq. (1)). Calculated θ_D for LiH and LiF systems are listed in Table I with their corresponding room temperature κ values. The θ_D values generally reflect the low frequency behavior of the acoustic modes in Figs. 1 and 2. From this alone, we expect the LiH systems to have higher κ than the LiF systems, which is indeed the case for LiH; however, the LiF calculated room temperature κ values are higher than the Li^2H values. Further, all of the calculated θ_D values here are higher than those previously calculated for Si, Ge, and BAs (707 K, 415 K, and 716 K) [64], with corresponding calculated room temperature κ values significantly higher (145 W/m-K, 60 W/m-K, and 2240 W/m-K, respectively) than the LiH and LiF systems here. This suggests that the dominant feature governing lattice thermal transport is phonon scattering resistance.

Phonon-isotope scattering via mass perturbation of the varying Li isotopes was included only in the calculation of κ values in Fig. 6 and Table I for LiH, Li^2H, and LiF; ^{6}Li and ^{7}Li were considered isotopically pure. As expected, the lack of mass disorder scattering in ^{7}LiF,^{7}LiH, and $^6Li^2H$ gives κ values higher than the corresponding naturally occurring Li systems (see Table I). However, the isotopically pure ^{6}LiF,^{6}LiH, and $^7Li^2H$ cases have lower κ values despite lacking this phonon-isotope scattering. This suggests that changes in the three-phonon scattering phase space with Li isotope enrichment induces more intrinsic resistance in these systems than the mass disorder scattering in the natural materials.

TABLE II. Calculated thermal conductivities (κ) for LiH and LiF at $T = 300$ K and $T = 600$ K for IFCs determined using different LDA lattice constants. a_0 is the calculated equilibrium lattice constant, and a (300 K) and a (600 K) include the effects of lattice expansion, as determined from Eq. (2) for their respective temperatures. For comparison, measured data are also shown. Bold numbers designate κ values for which the temperature used in the calculation matches the lattice parameter temperature. Calculated lattice constants for LiH are $a_0 = 3.894$ Å, $a(300\text{ K}) = 4.004$ Å and $a(600\text{ K}) = 4.048$ Å; for LiF, they are $a_0 = 3.886$ Å, $a(300\text{ K}) = 3.951$ Å, and $a(600\text{ K}) = 3.999$ Å.

	κ [a_0] (W/m-K)	κ [a(300 K)] (W/m-K)	κ [a(600 K)] (W/m-K)	κ [measured] (W/m-K)
LiH T = 300 K	25.51	**23.00**	20.29	12.47[a]
LiH T = 600 K	11.72	10.73	**9.35**	6.24[b]
LiF T = 300 K	22.42	**14.59**	10.55	14.09[c]
LiF T = 600 K	10.63	6.94	**5.07**	6.19[c]

[a]Reference [49]. The measurement was taken at 327 K.
[b]Reference [49].
[c]Reference [55].

To understand the intrinsic resistance from three-phonon interactions, we characterize scattering processes into four types: *aaa*, *aao*, *aoo*, and *ooo*, where *aaa* involves three acoustic phonons, *aao* involves two acoustic, and one optic phonon, etc. These scatterings can be generally correlated to features of the phonon dispersions by considering the effects of the conservation conditions, energy conservation in particular, on the phase space and thus the phonon lifetimes: (i) proximity of the acoustic branches (bunching) dictates possible *aaa* processes [64]; (ii) a frequency gap between acoustic and optic branches (*a-o* gap) dictates possible *aao* processes [6]; (iii) optic bandwidth (relative to overall acoustic frequency scale) and dispersion dictates possible *aoo* processes [65,66]; and (iv) energy conservation forbids *ooo* processes in most systems, including LiH and LiF here.

Despite having significant mass differences between the constituent atoms, these systems have little or no *a-o* gaps, characteristic of the ionic rock salt bonding structure. Thus, *aao* scattering is expected to be appreciable in these systems, as it is in other small *a-o* gap materials [6,67]. The acoustic branches of each system are bunched together throughout much of the Brillouin zone, so *aaa* scattering is expected to be relatively weak. To characterize this bunching, we calculate $(\omega_{\text{LA}}(X) - \omega_{\text{TA}}(\text{X}))/\omega_{\text{LA}}(X)$ composed of the transverse acoustic (TA) and longitudinal acoustic (LA) frequencies calculated at the X point. This gives values of 0.23 and 0.25 for all LiH and LiF systems, respectively. For comparison, Si has a value of 0.67 (with appreciable *aaa* scattering), and BAs has a value of 0.40 (with a small *aaa* scattering phase space) [64]. All systems have very large longitudinal optical–transverse optical (LO-TO) splittings and significant optic bandwidth with branch dispersion throughout this bandwidth. These features are also characteristics of ionic rock salt structures and were recently shown to contribute to strong *aoo* scattering and reduced κ contributions from acoustic modes in rock salt Pb X [65] and antifluorite Li_2X [66] (X = S, Se, Te). In contrast, for zincblende structures, *aoo* scattering is not important for determining κ. In Table I, we characterize the optic bandwidth of LiH and LiF systems. Note that small values mean only low frequency acoustic phonons can participate in *aoo* scatterings, as dictated by conservation of energy, and values $\geqslant 1$ mean all acoustic phonons can scatter in such processes. Nearly all of the acoustic modes of LiH and LiF systems can participate in *aoo* scattering processes, and ~70% of the acoustic modes in Li^2H are allowed. For comparison, only the lowest 40% and 35% of acoustic modes in Si and BAs, respectively, are allowed in *aoo* processes [66]. We note that this characterization does not include the additional restriction of crystal momentum conservation.

To further analyze the relationship of scattering rates and κ in these systems, Fig. 8 (LiH) and Fig. 9 (LiF) give the relative room temperature scattering rates for the TA and LA modes. The scattering rates for each phonon mode are scaled

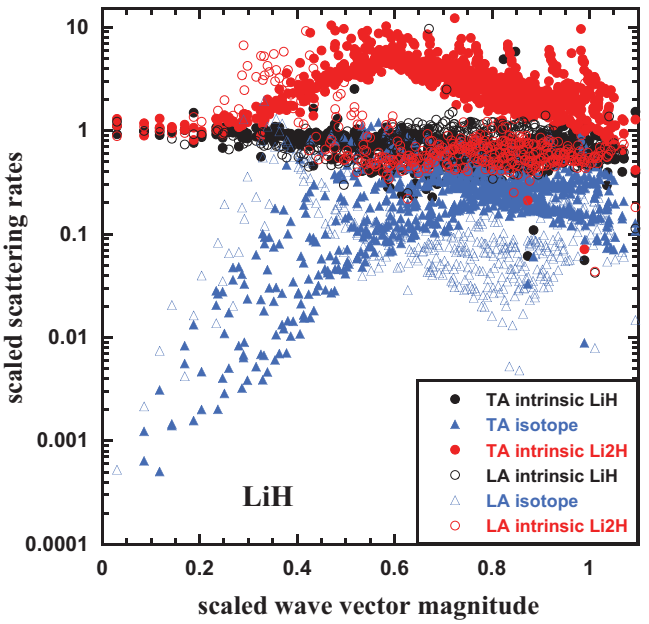

FIG. 8. Scaled acoustic mode scattering rates for LiH systems versus scaled wave vector magnitude at room temperature. The wave vectors are scaled by $2\pi/a$, while the scattering rates are scaled by the intrinsic phonon-phonon scattering rates calculated for isotopically pure ^{6}LiH. Solid symbols denote transverse acoustic (TA) modes, and hollow symbols denote longitudinal acoustic (LA) modes. Blue triangles give scaled isotope scattering, black circles give scaled intrinsic scattering for LiH, and red circles give scaled intrinsic scattering for Li^2H. All values above (below) one indicate scattering is stronger (weaker) than the intrinsic scattering of ^{6}LiH.

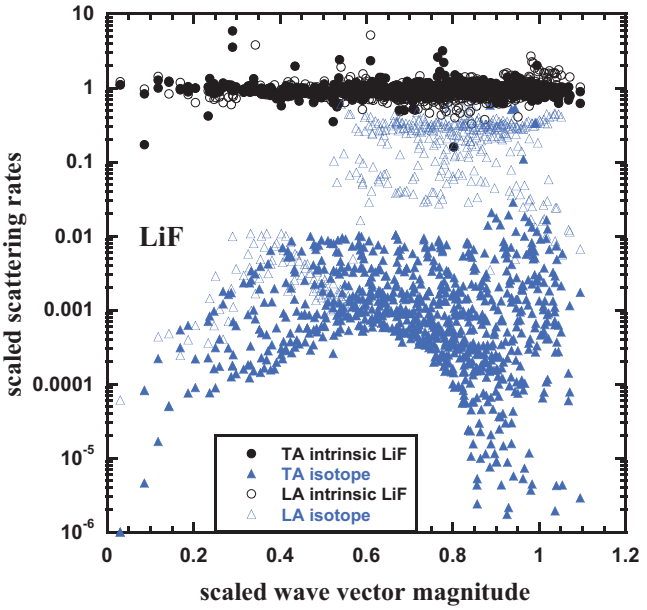

FIG. 9. Scaled acoustic mode scattering rates for LiF systems versus scaled wave vector magnitude at room temperature. The wave vectors are scaled by $2\pi/a$, while the scattering rates are scaled by the intrinsic phonon-phonon scattering rates calculated for isotopically pure ^{6}LiF. Solid symbols denote transverse acoustic (TA) modes, and hollow symbols denote longitudinal acoustic (LA) modes. Blue triangles give scaled isotope scattering, and black circles give scaled intrinsic scattering for LiF. All values above (below) one indicate scattering is stronger (weaker) than the intrinsic scattering of ^{6}LiF.

by the corresponding intrinsic phonon-phonon scattering rate for ^{6}LiH (Fig. 8) and ^{6}LiF (Fig. 9). Note that scaled values greater than one designate scattering rates that are greater than the intrinsic rates of the ^{6}Li systems (larger thermal resistance), and values less than one designate smaller scattering rates (smaller thermal resistance). First, phonon-isotope scattering is generally weaker than the intrinsic scattering in these systems at room temperature, especially for TA modes in the LiF systems. Thus, the additional mass disorder scattering is not playing a large role in determining κ. As temperature is decreased, the intrinsic phonon-phonon scattering becomes weaker, while the phonon-isotope scattering is unchanged thus giving the isotope-driven differences in peak κ in Fig. 6 for LiF. Next, the intrinsic scattering for LiH and LiF is generally weaker (though nominally so) than in ^{6}LiH and ^{6}LiF, respectively. More specifically, the acoustic modes of ^{6}LiH are higher than those in LiH, while the optic modes are unaltered (Fig. 2). This allows for increased coupling of the heat-carrying acoustic phonons with the optic phonons due to a smaller *a-o* gap in ^{6}LiH and, thus, reduction of their lifetimes. The weaker intrinsic scattering in ^{6}LiH and ^{6}LiF coupled with weak phonon-isotope scattering leads to the unusual behavior of lower κ in the isotopically pure ^{6}Li systems compared to their natural counterparts, despite having increased Debye temperatures (see Table I). For Li^2H, the intrinsic scattering of the TA modes is significantly larger than that of ^{6}LiH due to increased interactions of these phonons with the much lower frequency optic modes present in Li^2H, ultimately giving lower κ in the Li^2H system.

Finally, Slack [48] explained the low κ of LiH, despite being a simple material composed of light atoms, in terms of a relatively large value for its average Grüneisen parameter $\bar{\gamma}$ (defined in the Appendix), which gives a measure of lattice anharmonicity. Indeed, the calculated $\bar{\gamma}$ for the LiH systems is 1.1, larger than typical zincblende material values of ~0.7 [48]. The LiF systems have significantly larger $\bar{\gamma}$ with values of 1.83. Though $\bar{\gamma}$ has a reasonable correlation with the lower κ values for these systems when compared with typical zincblende materials, we note that this measure of the anharmonicity does not account for the important effects of fundamental conservations conditions toward limiting intrinsic phonon-phonon scattering.

IV. SUMMARY AND CONCLUSIONS

Using a first principles BPE approach, we characterized the effects of isotope variance on lattice thermal transport in ultra-low-mass compound materials LiH and LiF. In such light element systems, mass fluctuation not only modifies thermal conductivity via phonon-isotope scattering but also modulates the intrinsic κ via changes in the phonon dispersions of the optic branches (for H variance in LiH and Li variance in LiF systems) and to the acoustic branches (for Li variance in LiH systems). Isotope variation gives significant differences in optic phonon frequencies when comparing LiH and Li^2H and moderate differences in acoustic frequencies when comparing LiF and ^{6}LiF. These changes in the phonon dispersion give increased phase space for scattering of acoustic phonons by optic modes and lead to the unusual case of lower κ values in isotopically pure ^{6}LiH, $^7Li^2H$, and ^{6}LiF than in their counterparts with natural isotope abundances and mass disorder scattering. Good agreement of calculated and measured κ was obtained over a wide temperature range for LiF, however, not so for LiH. Phonon dispersions and scattering rates were compared, and the relatively important effect of lattice expansion with temperature on the calculated dispersions and thermal conductivities of these systems was discussed. Variation of intrinsic thermal resistance with isotope engineering is possible in these light atom systems, though the relative differences are small.

ACKNOWLEDGMENTS

L.L. acknowledges support from the U.S. Department of Energy, Office of Science, Office of Basic Energy Sciences, Materials Sciences and Engineering Division and the National Energy Research Scientific Computing Center (NERSC), a DOE Office of Science User Facility supported by the Office of Science of the U.S. Department of Energy under Contract No. DE-AC02-05CH11231.

APPENDIX

1. Calculation details

The coefficient of linear thermal expansion (α) is determined from [40]:

$$\alpha = \frac{1}{3B}\sum_{\vec{q}j} C_{\vec{q}j}\gamma_{\vec{q}j}, \tag{A1}$$

where B is the bulk modulus, $C_{\vec{q}j} = \hbar\omega_{\vec{q}j}(\partial n^0_{\vec{q}j}/\partial T)/V$ is the volume normalized mode heat capacity, $n^0_{\vec{q}j}$ is the equilibrium Bose distribution, $\omega_{\vec{q}j}$ is the frequency for phonon with wave vector $\vec{q}$ in branch j, and V is the crystal volume. $\gamma_{\vec{q}j}$ are the mode Grüneisen parameters given as [40]

$$\begin{aligned}\gamma_{\vec{q}j} &= -\frac{V}{\omega_{\vec{q}j}}\frac{d\omega_{\vec{q}j}}{dV} \\ &= -\frac{1}{6\omega^2_{\vec{q}j}}\sum_{k,l'k',l''k''}\sum_{\alpha\beta\gamma}\Phi_{\alpha\beta\gamma}(0k,l'k',l''k'') \\ &\quad\times\frac{\varepsilon^{j\vec{q}*}_{\alpha k}\varepsilon^{j\vec{q}}_{\beta k'}}{\sqrt{m_k m_{k'}}}e^{i\vec{q}\cdot\vec{R}_{l'}}r_{l''k''\gamma},\end{aligned} \tag{A2}$$

where lk designates the kth atom in the lth unit cell, $\varepsilon^{j\vec{q}}_{\alpha k}$ is the αth component of the phonon eigenvector, $\vec{R}_l$ is the lattice vector of the lth unit cell, $r_{lk\alpha}$ is the αth component of the vector locating the kth atom in the lth unit cell, m_k is the mass of the kth atom, and $\Phi_{\alpha\beta\gamma}(lk,l'k',l''k'')$ are the third order anharmonic IFCs. The measured values of the bulk moduli for LiH [33] and LiF [34] were used in Eq. (A1). The average Grüneisen parameters are calculated as

$$\bar{\gamma} = \sum_{\vec{q}j} C_{\vec{q}j}\gamma_{\vec{q}j} \Big/ \sum_{\vec{q}j} C_{\vec{q}j}. \tag{A3}$$

The Debye temperature, θ_D, is given by

$$\theta_D = \frac{\hbar}{k_B}v_D\sqrt[3]{\frac{6\pi^2 N}{V}} \tag{A4}$$

$$v_D^{-3} = \frac{1}{3}v_{\mathrm{LA}}^{-3} + \frac{2}{3}v_{\mathrm{TA}}^{-3}, \tag{A5}$$

where k_B and $\hbar$ are the Boltzmann and reduced Planck constants, N is the number of atoms, and v_{LA} and v_{TA} are the longitudinal and transverse sound velocities in the $\Gamma \rightarrow X$ direction.

2. Supplemental phonon dispersions

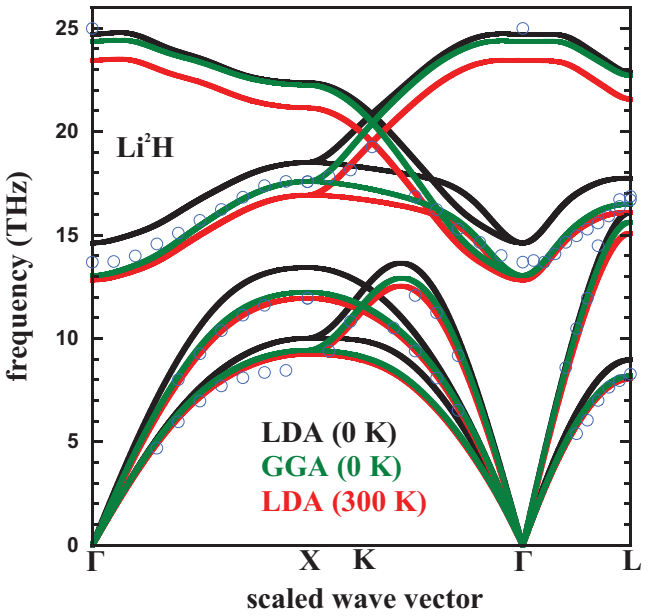

FIG. 10. Calculated phonon dispersions in high symmetry directions for Li^2H with energy minimized lattice constants ($T = 0$ K) for GGA (green curves, $a = 3.947$ Å), for LDA (black curves, $a = 3.894$ Å), and for LDA at $T = 300$ K (red curves, $a = 4.004$ Å) compared to measured data (blue circles, $a_{\mathrm{exp}} = 4.083$ Å) [36].

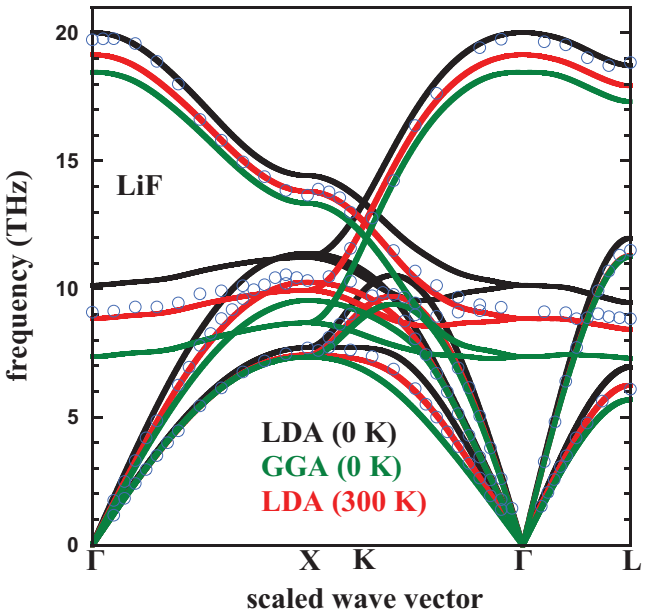

FIG. 11. Calculated phonon dispersions in high symmetry directions for LiF with energy minimized lattice constants ($T = 0$ K) for GGA (green curves, $a = 4.005$ Å), for LDA (black curves, $a = 3.886$ Å), and for LDA at $T = 300$ K (red curves, $a = 3.951$ Å) compared to measured data (blue circles, $a_{\mathrm{exp}} = 4.027$ Å) [37].

[1] T. H. Geballe and G. W. Hull, Phys. Rev. **110**, 773 (1958).
[2] J. R. Olson, R. O. Pohl, J. W. Vandersande, A. Zoltan, T. R. Anthony, and W. F. Banholzer, Phys. Rev. B **47**, 14850 (1993).
[3] L. Wei, P. K. Kuo, R. L. Thomas, T. R. Anthony, and W. F. Banholzer, Phys. Rev. Lett. **70**, 3764 (1993).
[4] C. W. Chang, A. M. Fennimore, A. Afanasiev, D. Okawa, T. Ikuno, H. Garcia, Deyuu Li, A. Majumdar, and A. Zettl, Phys. Rev. Lett. **97**, 085901 (2006).
[5] S. Chen, Q. Wu, C. Mishra, J. Kang, H. Zhang, K. Cho, W. Cai, A. A. Balandin, and R. S. Ruoff, Nat. Mat. **11**, 203 (2012).
[6] L. Lindsay, D. A. Broido, and T. L. Reinecke, Phys. Rev. Lett. **109**, 095901 (2012).
[7] L. Lindsay, D. A. Broido, and T. L. Reinecke, Phys. Rev. B **88**, 144306 (2013).
[8] J. M. Zhang, T. Ruf, M. Cardona, O. Ambacher, M. Stutzmann, J.-M. Wagner, and F. Bechstedt, Phys. Rev. B **56**, 14399 (1997).
[9] I. Pomeranchuck, J. Phys. U.S.S.R. **5**, 237 (1942).
[10] S. I. Tamura, Phys. Rev. B **27**, 858 (1983).
[11] S. I. Tamura, Phys. Rev. B **30**, 849 (1984).
[12] F. H. Welch, Nucl. Eng. and Design **26**, 444 (1974).
[13] W. Shoushan, C. Goulong, W. Fang, L. Yuanfang, Z. Ziying, and Z. Jianhuan, Rad. Prot. Dosimetry **14**, 223 (1986).
[14] F. Barkusky, C. Peth, K. Mann, T. Feigl, and N. Kaiser, Rev. Sci. Instru. **76**, 105102 (2005).
[15] J. Uhlíř, J. Nuc. Mat. **360**, 6 (2007).
[16] R. E. Peierls, *Quantum Theory of Solids* (Oxford University Press, London, 1955).
[17] J. M. Ziman, *Electrons and Phonons* (Oxford University Press, London, 1960).
[18] G. P. Srivastava, *The Physics of Phonons* (Taylor and Francis Group LLC, New York, 1990).
[19] H. B. G. Casimir, Physica **5**, 495 (1938).
[20] M. Omini and A. Sparavigna, Phys. Rev. B **53**, 9064 (1996).
[21] M. Omini and A. Sparavigna, Nuovo Cimento Soc. Ital. Fis., D **19**, 1537 (1997).
[22] S. Baroni, S. Gironcoli, A. D. Corso, and P. Giannozzi, Rev. Mod. Phys. **73**, 515 (2001).
[23] http://www.quantum-espresso.org.
[24] P. Giannozzi, S. Baroni, N. Bonini, M. Calandra, R. Car, C. Cavazzoni, D. Ceresoli, G. L. Chiarotti, M. Cococcioni, I. Dabo, A. D. Corso, S. Gironcoli, S. Fabris, G. Fratesi, R. Gebauer, U. Gerstmann, C. Gougoussis, A. Kokalj, M. Lazzeri, L. Martin-Samo *et al.*, J. Phys.: Condens. Matter **21**, 395502 (2009).
[25] P. Hohenberg and W. Kohn, Phys. Rev. **136**, B864 (1964).
[26] W. Kohn and L. J. Sham, Phys. Rev. **140**, A1133 (1965).
[27] N. Troullier and J. L. Martins, Phys. Rev. B **43**, 1993 (1991).
[28] See Supplemental Material at http://link.aps.org/supplemental/10.1103/PhysRevB.94.174304 for GGA and LDA input files and calculated IFCs.
[29] J. L. Anderson, J. Nasise, K. Philipson, and F. E. Pretzel, J. Phys. Chem. Sol. **31**, 613 (1970).
[30] C. A. Hutchison and H. L. Johnston, J. Am. Chem. Soc. **62**, 3165 (1940).
[31] P. Haas, F. Tran, and P. Blaha, Phys. Rev. B **79**, 085104 (2009).
[32] P. B. Allen, Phil. Mag. B **70**, 527 (1994).
[33] J. M. Besson, G. Weill, G. Hamel, R. J. Nelmes, J. S. Loveday, and S. Hull, Phys. Rev. B **45**, 2613 (1992).
[34] M. P. Tosi, Sol. St. Phys. **16**, 1 (1964).
[35] H. Kuwamoto and D. E. Holmes, J. App. Phys. **59**, 656 (1986).
[36] J. L. Verble, J. L. Warren, and J. L. Yarnell, Phys. Rev. **168**, 980 (1968).
[37] G. Dolling, H. G. Smith, R. M. Nicklow, P. R. Vijayaraghavan, and M. K. Wilkinson, Phys. Rev. **168**, 970 (1968).
[38] H. Jex, J. Phys. Chem. Sol. **35**, 1221 (1974).
[39] W. Brückner, K. Kleinstück, and G. R. E. Schulze, Phys. Status Solidi **14**, 297 (1966).
[40] J. Fabian and P. B. Allen, Phys. Rev. Lett. **79**, 1885 (1997).
[41] B. Müller, Goethe University Frankfurt, 1973.
[42] J. E. Rapp and H. D. Merchant, J. Appl. Phys. **44**, 3919 (1973).
[43] V. A. Eücken and W. Dannöhl, Z. Elektrochem. **40**, 819 (1934).
[44] P. D. Pathak, N. V. Pandya, and M. P. Ghaduli, Indian J. Phys. **37**, 293 (1963).
[45] S. S. Sharma, Proc. Indian Acad. Sci. A **32**, 268 (1950).
[46] G. K. White, Proc. R. Soc. A **286**, 204 (1965).
[47] B. Yates and C. H. Panter, Proc. Phys. Soc. Lond. **80**, 373 (1962).
[48] G. A. Slack, J. Phys. Chem. Sol. **34**, 321 (1973).
[49] J. B. Vetrano, Batelle Memorial Institute 1957 (unpublished), quoted by C. E. Messer and T. B. P. Gibb, Jr., in U.S. Atom Energy Comm. Rept. NYO-8022 (1957).
[50] I. B. Fieldhouse, J. C. Hedge, and J. I. Lang, WADC Technical Report TR-58-274 (1958).
[51] L. Manning and D. J. McKee, General Electric Nuclear Materials and Propulsion Operation, U.S. Atom. Energy Comm. Report Apex-744 (1961).
[52] P. D. Thacher, Phys. Rev. **156**, 975 (1967).
[53] R. Berman and J. C. F. Brock, Proc. R. Soc. London A **289**, 46 (1965).
[54] S. J. Rogers, Phys. Rev. B **3**, 1440 (1971).
[55] A. V. Petrov, N. S. Tsypkina, and V. E. Seleznev, High Temp.-High. Press. **8**, 536 (1976).
[56] J. Garg, N. Bonini, B. Kozinsky, and N. Marzari, Phys. Rev. Lett. **106**, 045901 (2011).
[57] W. Li, L. Lindsay, D. A. Broido, D. A. Stewart, and N. Mingo, Phys. Rev. B **86**, 174307 (2012).
[58] P. Debye, Annalen der Physik **344**, 789 (1912).
[59] C. Kittel, *Introduction to Solid State Physics*, 7th ed. (John Wiley and Sons, Inc., Hoboken, 1996).
[60] T. Feng and X. Ruan, Phys. Rev. B **93**, 045202 (2016).
[61] D. A. Broido, M. Malorny, G. Birner, N. Mingo, and D. A. Stewart, Appl. Phys. Lett. **91**, 231922 (2007).
[62] A. Ward, D. A. Broido, D. A. Stewart, and G. Deinzer, Phys. Rev. B **80**, 125203 (2009).
[63] I. M. Mills, J. Phys. Chem. **88**, 532 (1984).
[64] L. Lindsay, D. A. Broido, and T. L. Reinecke, Phys. Rev. Lett. **111**, 025901 (2013).
[65] S. Lee, K. Esfarjani, T. F. Luo, J. W. Zhou, Z. T. Tian, and G. Chen, Nat. Commun. **5**, 3525 (2014).
[66] S. Mukhopadhyay, L. Lindsay, and D. S. Parker, Phys. Rev. B **93**, 224301 (2016).
[67] L. Lindsay, D. A. Broido, and T. L. Reinecke, Phys. Rev. B **87**, 165201 (2013).